Draft version August 22, 2013
Preprint typeset using LaTeX style emulateapj v. 08/22/09

THE HERSCHEL STRIPE 82 SURVEY (HERS): MAPS AND EARLY CATALOG†

M.P. Viero[1,‡], V. Asboth[2], I. G. Roseboom[3], G. Marsden[2], L. Moncelsi[1], E. Mentuch Cooper[4], M. Zemcov[1,5], G. Addison[2], A.J. Baker[6], A. Beelen[7], J. Bock[1,5], C. Bridge[1], A. Conley[8], M. J. Devlin[9], O. Doré[5,1], D. Farrah[10], S. Finkelstein[4], A. Font-Ribera[11,12], J. E. Geach[13], K. Gebhardt[4], A. Gill[8], J. Glenn[14,8], A. Hajian[15], M. Halpern[2], S. Jogee[4], P. Kurczynski[6], A. Lapi[16,17], M. Negrello[18], S. J. Oliver[19], C. Papovich[20], R. Quadri[21,22], N. Ross[12], D. Scott[2], B. Schulz[1,23], R. Somerville[6], D. N. Spergel[24], R. Wechsler[25], J. D. Vieira[1]

Draft version August 22, 2013

ABSTRACT

We present the first set of maps and band-merged catalog from the *Herschel* Stripe 82 Survey (HerS). Observations at 250, 350, and 500 µm were taken with the Spectral and Photometric Imaging Receiver (SPIRE) instrument aboard the *Herschel Space Observatory*. HerS covers 79 deg^2 along the SDSS Stripe 82 to a depth of 13.0, 12.9, and 14.8 mJy beam^{-1} (including confusion) at 250, 350, and 500 µm, respectively. The band-merged catalog contains 2.7×10^4 sources detected at a significance of $\gtrsim 5\sigma$. HerS was designed to measure correlations with external tracers of the dark matter density field — either point-like (i.e., galaxies selected from radio to X-ray) or extended (i.e., clusters and gravitational lensing) — in order to measure the bias and redshift distribution of intensities of infrared-emitting dusty star-forming galaxies and AGN. By locating HeRS in Stripe 82, we maximize the overlap with available and upcoming cosmological surveys. The maps and catalog are available at `http://www.astro.caltech.edu/hers/`.

Subject headings: cosmology: observations, submillimeter: galaxies – infrared: galaxies – galaxies: evolution – large-scale structure of universe

1. INTRODUCTION

The cosmic infrared background (CIB) traces the star-formation history of the Universe; roughly half the emission of young stars appears in the ultraviolet and optical, while the rest is absorbed by dust and then emitted at far-infrared wavelengths (Puget et al. 1996; Fixsen et al. 1998; Hauser & Dwek 2001; Dole et al. 2006). Over the last decade a key goal of far-IR/submillimeter astronomy has been to identify the galaxies that produce the CIB. Recent deep surveys with the Balloon-borne Large Aperture Submillimeter Telescope (BLAST; Devlin et al. 2009; Marsden et al. 2009; Pascale et al. 2009) and the *Herschel Space Observatory* (H-ATLAS, HerMES, PEP; Eales et al. 2010; Oliver et al. 2012; Lutz et al. 2011) as well as ground-based submillimeter facilities such as LABOCA (LESS; Weiß et al. 2009) and SCUBA-2 (Geach et al. 2013) have “resolved” over 80% of the CIB at submillimeter wavelengths, via direct counting of sources (Oliver et al. 2010; Geach et al. 2013), *P(D)* techniques (Glenn et al. 2010), and stacking (Dole et al. 2006; Berta et al. 2011; Béthermin et al. 2012; Viero et al. 2012, 2013b). The resolution of this

‡ Email: marco.viero@caltech.edu
† Herschel is an ESA space observatory with science instruments provided by European-led Principal Investigator consortia and with important participation from NASA.
[1] California Institute of Technology, 1200 E. California Blvd., Pasadena, CA 91125
[2] Department of Physics & Astronomy, University of British Columbia, 6224 Agricultural Road, Vancouver, BC V6T 1Z1, Canada
[3] Institute for Astronomy, University of Edinburgh, Royal Observatory, Blackford Hill, Edinburgh EH9 3HJ, UK
[4] Department of Astronomy, The University of Texas at Austin, Austin, TX 78712
[5] Jet Propulsion Laboratory, 4800 Oak Grove Drive, Pasadena, CA 91109
[6] Department of Physics and Astronomy, Rutgers, The State University of New Jersey, 136 Frelinghuysen Rd, Piscataway, NJ 08854
[7] Institut d'Astrophysique Spatiale (IAS), bâtiment 121, Université Paris-Sud 11 and CNRS (UMR 8617), 91405 Orsay, France
[8] Center for Astrophysics and Space Astronomy 389-UCB, University of Colorado, Boulder, CO 80309
[9] Department of Physics and Astronomy, University of Pennsylvania, Philadelphia, PA 19104
[10] Department of Physics, Virginia Tech, Blacksburg, VA 24061
[11] Institute of Theoretical Physics, University of Zurich, Winterthurerstrasse 190, 8057 Zurich, Switzerland
[12] Lawrence Berkeley National Laboratory, 1 Cyclotron Road, Berkeley, CA 94720
[13] Centre for Astrophysics Research, Science & Technology Research Institute, University of Hertfordshire, Hatfield, AL10 9AB, UK
[14] Dept. of Astrophysical and Planetary Sciences, CASA 389-UCB, University of Colorado, Boulder, CO 80309
[15] Canadian Institute for Theoretical Astrophysics, University of Toronto, Toronto, ON M5S 3H8, Canada
[16] Dip. Fisica, Univ. ‘Tor Vergata’, Via Ricerca Scientifica 1, 00133 Roma, Italy
[17] Astrophysics Sector, SISSA, Via Bonomea 265, 34136 Trieste, Italy
[18] INAF, Osservatorio Astronomico di Padova, Vicolo Osservatorio 5, I-35122 Padova, Italy
[19] Astronomy Centre, Dept. of Physics & Astronomy, University of Sussex, Brighton BN1 9QH, UK
[20] George P. and Cynthia Woods Mitchell Institute for Fundamental Physics and Astronomy, Department of Physics and Astronomy, Texas A&M University, College Station, TX 77843
[21] Hubble Fellow
[22] Carnegie Observatories, Pasadena, CA 91101
[23] Infrared Processing and Analysis Center, MS 100-22, California Institute of Technology, JPL, Pasadena, CA 91125
[24] Joseph Henry Laboratories of Physics, Jadwin Hall, Princeton University, Princeton, NJ 08544
[25] Kavli Institute for Particle Astrophysics and Cosmology and Department of Physics, Stanford University, 382 Via Pueblo Mall, Stanford, CA 94305

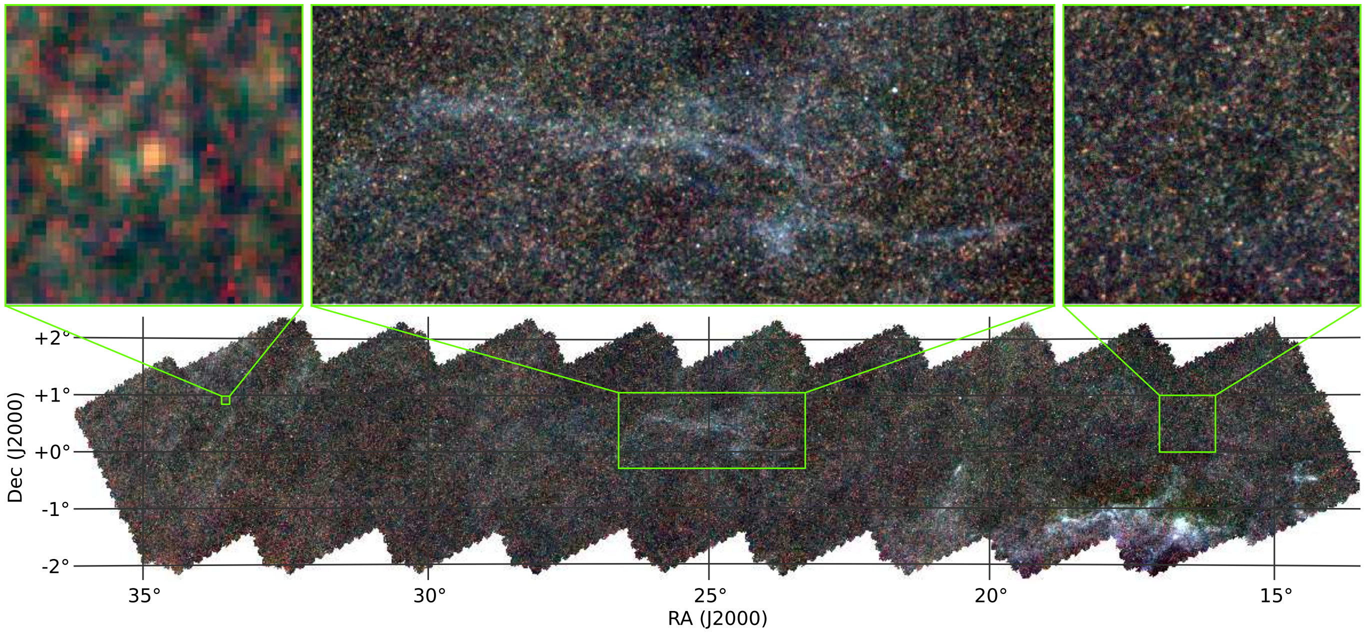

Figure 1. Three-color image of the HerS field with 250, 350, and 500 μm as blue, green, and red, respectively. Note that 250 and 350 μm maps were convolved so that all three maps have the same angular resolution. **Left Panel:** A high-redshift candidate "red peaker", with $S_{250} < S_{350} < S_{500}$, such that its SED suggests it lies somewhere between z of 3 and 7. **Center Panel:** A foreground cloud of Galactic cirrus (see § 5), with column densities reaching $N_{\rm H} \sim 4.5 \times 10^{21}\,{\rm cm}^{-2}$. **Right Panel:** A typical $1^\circ \times 1^\circ$ "blank field", which contains mostly dusty star-forming galaxies at intermediate to high redshifts.

large fraction of the CIB into individual sources makes it clear that the CIB, at least near to its peak at $\sim 200\,\mu$m, is dominated by a moderate luminosity population (i.e., $L_{\rm IR} \leq 10^{12}\,{\rm L}_\odot$; Béthermin et al. 2011; Wang et al. 2013) in the broad redshift interval $1 \leq z \leq 3$ (e.g., Viero et al. 2013a). Additionally, measurements of the CIB power spectrum (e.g., Viero et al. 2009; Amblard et al. 2011; Planck Collaboration et al. 2011c; Viero et al. 2013b) yield estimates of the source clustering properties.

While the determination of these broad characteristics represents a remarkable achievement, much remains to be done to link the CIB, and the infrared (IR) luminous galaxies which make it up, to the general galaxy population. This goal requires determining the multi-wavelength characteristics of galaxies detected at far-IR/submillimeter wavelengths, and hence the physical properties that these wavelengths probe, e.g., rest-frame optical light tracing stellar mass, X-ray tracing black hole accretion, etc. A major complication is that the confusion-limited sensitivity of single-dish far-IR/submillimeter facilities is such that only the most luminous sources (i.e. $L_{\rm IR} \geq 10^{12}\,{\rm L}_\odot$) can be individually detected in the key redshift range $1 \leq z \leq 3$. Interferometric facilities like ALMA are not limited in this way, although their small fields of view (e.g. $\ll 1$ arcmin^2) means that large blind surveys of the IR-galaxy population are inefficient and prohibitively expensive. To characterize the physical properties of the galaxies that dominate the CIB will require the use of statistical techniques, i.e. stacking or similar (Devlin et al. 2009; Marsden et al. 2009; Pascale et al. 2009; Kurczynski et al. 2012; Viero et al. 2012, 2013a; Roseboom et al. 2012), and hence very large numbers ($>$ 100,000) of galaxies detected at wavelengths with higher resolution (typically optical/near-IR).

Motivated by the importance of the CIB and the need to have large multi-wavelength surveys to understand its properties, we have conducted the *Herschel* Stripe 82 Survey (HerS; Figure 1). HerS consists of 79 deg^2 of contiguous imaging with the SPIRE instrument (Griffin et al. 2010) on the *Herschel Space Observatory* (Pilbratt et al. 2010) to roughly the confusion limit (~ 7 mJy at the wavelengths 250, 350, and 500 μm; Nguyen et al. 2010). Crucially, HerS is positioned to overlap with a rich array of both existing and planned data in the "Stripe 82" field, including: The SDSS-III's Baryon Oscillation Spectroscopic Survey (BOSS; Eisenstein et al. 2011), VICS82 (VISTA+CFHT Stripe 82 survey; Geach et al. in prep.), VISTA-VIKING (Emerson et al. 2004), VLA-Stripe82 (Hodge et al. 2011), The Hobby-Eberly Telescope Dark Energy Experiment (HETDEX; Hill et al. 2008), The *Spitzer*-HETDEX Exploratory Large Area Survey (SHELA; Papovich et al. 2012), The *Spitzer*-IRAC Equatorial Survey (SpIES; Richards et al. 2012), Hyper Suprime-Cam (HSC; Miyazaki et al. 2012), and The Atacama Cosmology Telescope (ACT; Sievers et al. 2013) surveys. The combination of SHELA/SpIES, which are *Spitzer*-warm IRAC surveys of Stripe 82, and HETDEX, a wide-area spectroscopic survey targeting emission lines at $z > 2$, will detect hundreds of thousands of galaxies and provide the key information required to interpret the HerS images.

In addition to these large statistical analyses, the large area of HerS adds an additional 79 deg^2 to the existing wide-area H-ATLAS and HerMES surveys to identify and study sources that are "rare" on the sky. The HerS field contains tens of nearby luminous IR galaxies (LIRGs; $L_{\rm IR} \geq 10^{11}\,{\rm L}_\odot$) that are close enough to be resolved by *Herschel* at 250 μm. Meanwhile, we expect to identify close to 100 distant ($z > 2$) galaxies with

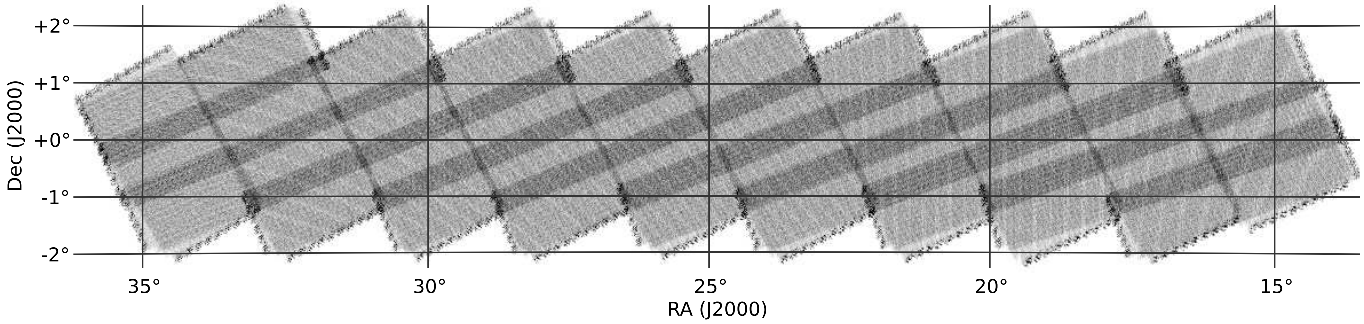

Figure 2. Coverage map of the 350 μm data. The majority of the map is covered twice, while the dark grey stripes are the regions covered three times. As the scan orientations of the telescope at the ecliptic are fixed irrespective of the observing season, this scan strategy was chosen to guarantee complete coverage of the area along the stripe.

very high observed luminosities, with many of these resulting from lensing by foreground galaxies (like those found in e.g. Negrello et al. 2010; Wardlow et al. 2012; Vieira et al. 2013). Finally, HerS will contain many thousands of LIRGs at intermediate redshifts, making it a rich dataset for the study of IR-luminous galaxy evolution since $z = 1$.

This paper describes the first release of HerS maps and catalog, including design strategy (§ 2), map-making and map properties (§ 3), and catalog construction and statistics (§ 4). Data are available at `http://www.astro.caltech.edu/hers/`.

2. SURVEY DESIGN

HerS was designed to optimize cross-correlation measurements with ancillary data sets. This objective requires two key ingredients: well understood ancillary data (preferably of high source density); and submillimeter maps covering large areas with faithful reconstruction of large scales. To satisfy the first criterion, the survey was located in Stripe 82 which, in addition to the numerous surveys already described, will uniquely be observed by both HETDEX and ACT. Furthermore, its equatorial location — visible from most ground-based telescopes — makes it well-placed to be a valuable legacy field in the future. Its location was driven by the relatively low Galactic cirrus foreground (e.g., $N_{\rm H} \sim 1.7 \times 10^{21}\,{\rm cm}^{-2}$; see § 3.5) with respect to the rest of the stripe. Combined with the HeLMS survey (the largest field in HerMES; Oliver et al. 2012), the full $\sim 150\,{\rm deg}^2$ of Stripe 82 with $N_{\rm H} \leq 3 \times 10^{21}\,{\rm cm}^{-2}$ has been imaged.

The second criterion — the need for large areas — is again due to source confusion. As shown in e.g., Acquaviva et al. (2008), the signal-to-noise ratio in cross-correlation measurements is proportional to the square root of $f_{\rm sky}$, or areal coverage, and is inversely proportional to the square root of the noise. For the case of maps observed with SPIRE, since the noise as a function of observing time quickly approaches the confusion limit, observation time is more optimally spent going wider rather than deeper. To reconstruct the largest scales, the maps were imaged in fast-scan mode ($60\,{\rm arcsec\,s}^{-1}$) and cross-linked with nearly orthogonal scans. The equatorial location of the field limited the orientations possible with the telescope. Coverage of the stripe, visible in the coverage map shown in Figure 2, was achieved in 21 scans over 34.5 hours of observing time. This scan pattern resulted in 10 stripes with additional coverage, i.e., 3 rather than 2 scans; we address in later sections how these deeper stripes affect the noise properties of the maps and completeness properties of the catalogs.

3. MAPS

Observations cover $79\,{\rm deg}^2$ in the equatorial Stripe 82, spanning 13° to 37° ($0^{\rm h}54^{\rm m}$ to $2^{\rm h}24^{\rm m}$) in RA, and $-2°$ to $2°$ in declination. Maps were made using the maximum likelihood mapmaker SANEPIC (Signal and Noise Estimation Procedure Including Correlations; Patanchon et al. 2008). This mapmaker is optimized for datasets where a large number of detectors observe the same area of the sky and the correlated (or common-mode) noise between the time-ordered data (TOD, or timestream) of these detectors cannot be ignored. The main source of this common-mode noise is the drift in temperature of the cooler bath surrounding the detector arrays. Instead of removing all large-scale variations with high-pass filtering, as many other mapmakers do, SANEPIC separates the low-frequency correlated noise from the sky signal, resulting in maps in which large-scale variations of the sky are better preserved.

Two sets of maps at 250, 350, and 500 μm were made in order to accommodate different science goals. For the first set, we used a tangent plane (TAN) projection with pixel sizes of 6, 8.333 and 12 arcseconds for the 250, 350 and 500 μm maps, respectively. These values are typical for SPIRE maps, chosen to correspond to roughly one-third of the size of the SPIRE beams (18.1, 25.2 and 36.6 arcsec full-width at half-maximum). Since the HerS field overlaps with the equatorial stripe observed by the Atacama Cosmology Telescope (ACT), we also made maps using the nominal ACT map projection for cross-analysis of the two data sets. These maps were made using a cylindrical equal-area (CEA) projection with pixel sizes of 29.7 arcsec in all three bands, corresponding to the nominal ACT pixel size.

3.1. *Data preprocessing*

The raw data from the bolometer arrays are stored as separate TODs for each detector. Before the data are fed into our mapmaker several preprocessing steps are applied to the raw TODs. We used the HIPE (Herschel Interactive Processing Environment; Ott 2010), version 11.0.1 mapmaking software package to convert the uncalibrated raw TODs into the so-called Level 1 format, which is the input format used by mapmakers. The preprocessing steps involve detecting jumps in the signal, flagging glitches, and correcting for the low-pass filter response of the electronics and for the bolometer time response. Calibration of the data also happens at this early processing stage. The Level 1 data are read in by the SMAP mapmaking software package (Levenson et al. 2010; Viero et al. 2013b) and exported to the format accepted by SANEPIC. SMAP also uses an additional iterative glitch detection algorithm during mapmaking, and the deglitching information can be re-used later. This existing deglitching-information from preliminary HerS maps created with SMAP is also applied to our TODs. For details of these preprocessing steps see appendix A of Viero et al. (2013b). Both the HIPE and SMAP pipelines have their own algorithms to remove temperature drifts on long timescales by fitting to thermistor TODs. Since SANEPIC is optimized to deal with large-scale correlated noise, we turn off the temperature drift removal step in HIPE and SMAP during preprocessing. The last preprocessing steps are applied by SANEPIC. A first-order polynomial is fit to and removed from each data segment, because the variations on timescales longer than the timestream itself can cause leakage during Fourier-transformation, which would introduce artifacts in our maps. SANEPIC fills any gaps in the TODs and the data segments are apodized at the edges over 50 samples. This measure is needed since the mapmaker assumes that the ends of each data segment are strongly correlated ("circular").

3.2. *Mapmaking*

The SANEPIC mapmaking method is described in detail in Patanchon et al. (2008); here we review the salient points. The timestream of a bolometer indexed by i can be modeled as

$$d_i(t) = \sum_p A_{ip}(t)s_p + n_i(t), \tag{1}$$

where t is the time when the sample was taken, s_p is the signal in pixel p of the map of the sky and $A_{ip}(t)$ is the pointing matrix, which gives the weight of the contribution of the signal in pixel p to the timestream of bolometer i at time t. We assert that s_p corresponds to the beam-convolved sky, in which case the pointing matrix tells us the position where bolometer i points on the sky at time t. The noise term $n_i(t)$, whose properties are assumed to be stationary, is the sum of two components: the uncorrelated noise between different detectors $\tilde{n}_i(t)$; and a common-mode signal, $\alpha_i c(t)$, seen by all detectors at a given time. This "noise" term is

$$n_i(t) = \tilde{n}_i(t) + \alpha_i c(t), \tag{2}$$

where $c(t)$ is the correlated noise which is the same for all detectors apart from a detector-dependent multiplicative factor α_i. The sky signal can be estimated from the detector TODs using maximum likelihood methods. The solution is given by

$$\hat{s} = (A^{\mathrm{T}}N^{-1}A)^{-1}A^{\mathrm{T}}N^{-1}d, \tag{3}$$

where N^{-1} represents the inverse of the time-domain noise covariance matrix. This can be calculated as

$$N^{-1} = \mathcal{F}^{-1}[P(\omega)^{-1}], \tag{4}$$

where $\mathcal{F}^{-1}$ represents the inverse Fourier-transformation and $P(\omega)$ is a matrix constructed from the auto- and cross-power spectra of the TODs, containing information about the detectors common-mode noise, in addition to the uncorrelated noise terms:

$$P^{-1}(\omega) = [\alpha\langle c(\omega)^{\dagger}c(\omega)\rangle\alpha^{t} + \langle\tilde{n}^{\dagger}(\omega)\tilde{n}(\omega)\rangle]^{-1}. \tag{5}$$

The inverse of the pixel-pixel noise covariance matrix, $N_{pp'}^{-1} = (A^T N^{-1} A)^{-1}$ is not calculated explicitly. The mapmaker uses an iterative algorithm based on the conjugate gradient method with preconditioner to find the maximum likelihood solution for the map. Usually a few hundred iterations are needed to reach convergence. The computational time scales with the square of the number of bolometers and also depends on the number of samples, n_s, in the TOD as $n_s\log(n_s)$. Our observations consist of 34.5 hours of data for each bolometer sampled at a frequency of 18.6 Hz. The 250 µm array has the largest number of bolometers (139) so the map created from this data has the longest processing time. Using eight 2.8 GHz processors (Intel Xeon X5560 CPUs) the mapmaker needs about 17 hours to reach convergence at 250 µm.

3.3. *Noise properties*

To examine the properties of the residual noise in our signal maps, we create jackknife difference maps. The timestream data are split into two halves and a separate map is made for each half. The difference map is then made by multiplying one of the maps by minus one and then averaging the two together. This process removes the astronomical signal and the jackknife difference map contains the same statistical noise properties as the coadded sky map. There are in principle several different ways to split the data in half, some more effective than others, but due to the shallow depth of the HerS we do not have all of the options as we would have with deeper maps. For example, since the field is only scanned once in each orthogonal direction, we cannot split the TODs into two halves based on observation time, and splitting the datasets by orthogonal scan-direction results in maps that have strong residual correlated noise along the scan directions, due to lack of cross-linking. A third way to split the data is to divide up the detector focal planes, and only use every second bolometer to make our maps. Even though this method gives the best coverage, at the nominal pixel sizes the resulting maps are still quite sparse, especially at 500 µm where the sampling density is the lowest. This problem is not present in the larger pixel-size maps corresponding to the ACT mapping, and after correcting for the effect of the bigger pixel size we recover values similar to those in the more finely sampled maps.

Instrumental noise is calculated by fitting a Gaussian to the pixel-histogram of the jackknife maps. We find that the noise is extremely well described by the Gaussian fit, deviating only at 500 µm by less than 2%, and that the deviation is explained by the non-uniformity in the samples per pixel arising from the sparseness of the array and the fact that we only cover each area with two scans. The resulting 1σ values in the TAN (CEA) maps are 11.9 (2.2), 11.4 (3.1), and 13.5 (5.4) mJy beam^{-1} at 250, 350 and 500 µm, respectively. Note that since the coverage of the HerS maps is not completely uniform (seen clearly in Figure 2), the noise levels where

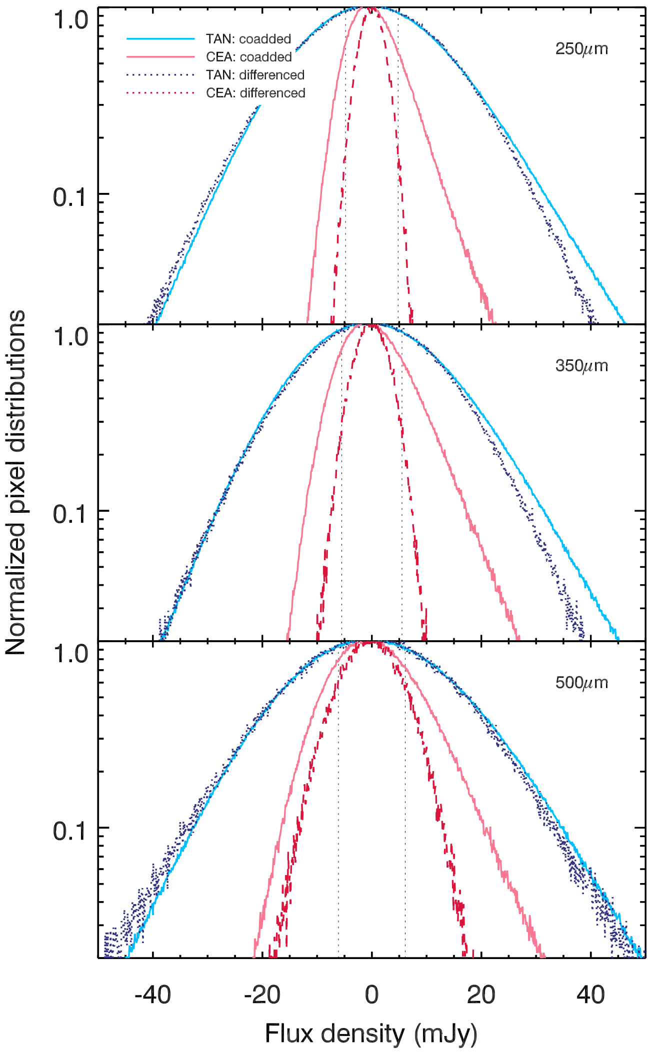

Figure 3. Pixel flux distributions of the coadded (i.e., the sky) and differenced jackknife maps, represented as solid and dotted lines, respectively, for both TAN (wider light/dark blue) and CEA (narrower red/pink) projections. Coadded maps include the entire data set in each band, while in the differenced maps the sky signal has been removed, leaving only instrumental noise. Coadded histograms are thus wider because they include confusion noise, represented by vertical dashed lines from Nguyen et al. (2010), as well as an excess compared with a Gaussian at brighter flux densities from resolved sources. Note that the TAN maps with its smaller pixels are dominated by instrumental noise, while the bigger pixel CEA maps have approximately equal contributions from instrument and confusion noise.

more than two orthogonal scans overlap is lower. In these deeper regions the noise levels are 10.7 (2.1), 10.3 (2.8), and 12.3 (4.9) mJy beam^{-1}, while in the shallower regions they are 13.3 (2.5), 12.7 (3.4), and 14.9 (6.0) mJy beam^{-1} at 250, 350 and 500 µm, respectively.

SANEPIC also creates an error map as an extension to the output products. This map gives an estimate of the variance of the noise in each pixel of the final map. Obtaining this error term correctly would require calculating the explicit pixel-pixel noise covariance matrix, but that operation is too computationally intensive and is never carried out during the iterative mapmaking. The error map SANEPIC creates is a first-order estimate of this noise, computed by neglecting the off-diagonal terms in

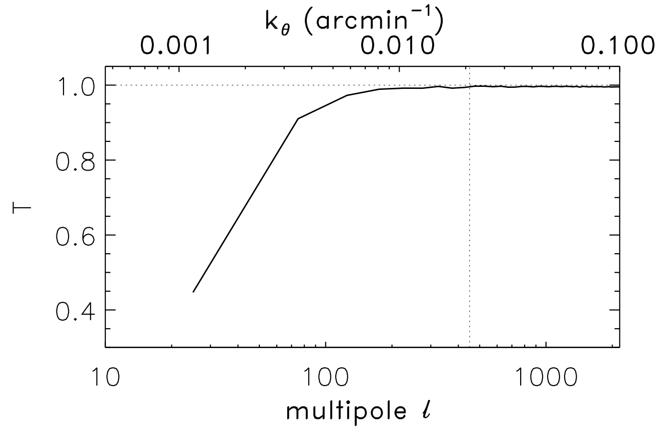

Figure 4. Transfer function, T, of the SANEPIC mapmaker, estimated with a Monte Carlo simulation as described in § 3.4. T is found to be approximately unity down to $\ell \sim 200$ (~ 1 deg), dropping to 0.5 at $\ell \sim 30$. The vertical dashed line represents the largest accessible scale, given the finite size of the survey, showing that effectively all scales in the map are reconstructed. Upper axis indicates $k_\theta \equiv \ell/(2\pi)$.

the inverse pixel-pixel noise covariance matrix, assuming that the final map only contains white noise. These determinations over-estimate the real residual noise values in the maps, but the error map can still be used to assign weights to each pixel in our final map.

3.4. *Transfer Function*

We investigate how reliable our mapmaker is in reconstructing large-scale structure on different angular scales. This assessment is made by creating simulated pure-signal maps, which are then reprojected into detector TODs and fed back into our mapmaker the same way as for the real data. The ratio of the azimuthally-averaged Fourier transform of the reconstructed map and the pure-signal input map gives us the mapmaker's transfer function. In the ideal case the ratio should be unity at all spatial scales. However, the mapmaker can introduce false signal to our maps, or remove existing power, which would appear as a deviation from unity in the transfer function. On the scales where the deviation from unity is not too large, we can correct for these effects. We created 100 pure signal maps with a Monte Carlo simulation using a power-law power spectrum resembling that of the cosmic infrared background without the cirrus. Figure 4 shows the resulting transfer function. The mapmaker can successfully reconstruct all large scales that are accessible in our maps. The simulated and reconstructed maps were made with the same pixel size, so the pixel window function does not have any effect here, and the transfer function remains unity on small scales. The transfer function only starts to drop for $\ell \lesssim 200$, corresponding to approximately half of the narrowest extent of our survey.

3.5. *Galactic Cirrus*

Thermal emission by diffuse interstellar dust in our Galaxy — the diffuse Galactic cirrus — can be described by a modified blackbody proportional to $\nu^\beta B(\nu)$, where $B(\nu)$ is the Planck function and β is the emissivity index, with temperatures ranging from 17 to 20 K in the most diffuse regions (e.g., Boulanger et al. 1996; Bracco et al.

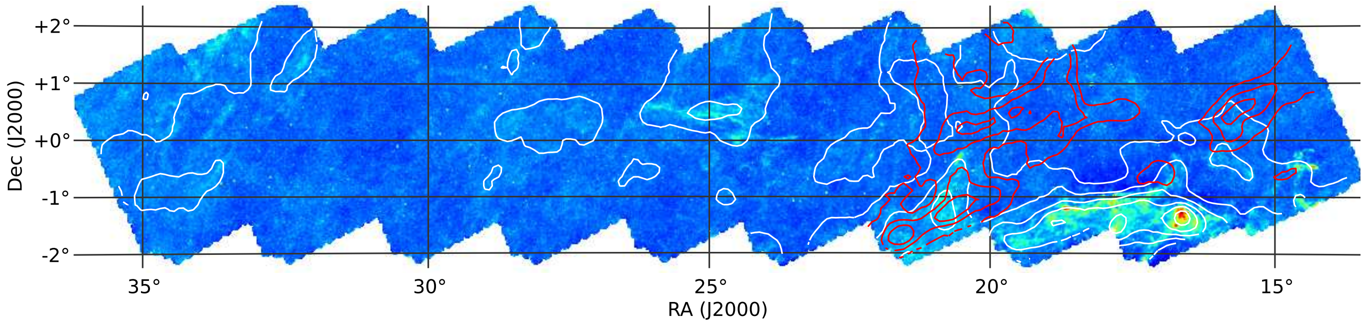

Figure 5. HerS 250 μm map, smoothed to 2 arcmin, overlaid with contours representing the column density of local velocity clouds (white) and IVCs (red), as traced by H I emission from GASS 21-cm data. Note that no HVCs appear in this field. White contours show $N_{\rm H}$ at 3.4, 4.2, 5.0, 5.8, 6.6, and $7.4 \times 10^{21}\,{\rm H\,cm^{-2}}$, while red contours show $N_{\rm H}$ at 0.5, 0.8, and $1.1 \times 10^{21}\,{\rm H\,cm^{-2}}$. The color scale ranges linearly from -25 (blue) to 80 mJy (red). The vast majority of the cirrus visible in HerS is attributable to the local velocity component.

2011), to as low as 14 K in dense regions where molecular hydrogen (H_2) can form (e.g., Netterfield et al. 2009; Planck Collaboration et al. 2011b), peaking in emission between 150 and 200 μm.

In diffuse regions, dust is well-traced by atomic hydrogen gas (H I) which emits at 21 cm and in the radio (e.g., Boulanger et al. 1996). H I data are available for HerS from the Parkes Galactic All-Sky Survey (GASS; McClure-Griffiths et al. 2009; Kalberla et al. 2010), a 1.4 GHz survey of Galactic atomic hydrogen emission, taken with the Parkes 64-m radio telescope, over > 20,000 deg^2. Publicly available data[28] are provided as velocity cubes, with effective angular resolution of 16′, and velocity resolution of $1.0\,{\rm km\,s^{-1}}$. Following Planck Collaboration et al. (e.g., 2011a), we divide the cubes by velocity with respect to the local frame of reference into local ($|v_{\rm LSR}| < 30\,{\rm km\,s^{-1}}$) and intermediate velocity clouds (IVCs; $|v_{\rm LSR}| > 30\,{\rm km\,s^{-1}}$). Note that no HVCs are visible in this field. We plot contours of the local and IVC components in Figure 5 (white and red contours, respectively), showing that the cirrus emission in HerS comes predominantly from the local velocity component.

For column densities of roughly $N_{\rm H} \lesssim 4 \times 10^{21}\,{\rm cm^{-2}}$, and on scales of an arcminute or less, this foreground is easily suppressed with a high-pass or matched filter (e.g., Chapin et al. 2011). High concentrations of H I (and potentially H_2) — such as that present in the bottom right corner of the HerS maps — present a greater challenge; we describe our filtering method for point source identification in § 4.

4. CATALOG

4.1. *Catalogue production*

Point source catalogs across the HerS field in the three SPIRE bands were produced using a three-step process: map filtering (to remove large-scale Galactic cirrus); source identification; and source extraction. We now describe the details of each of these steps in turn.

The HerS maps are filtered using a tapered high-pass filter, that begins to remove power on scales larger than 10 arcmin. Specifically, we take the 2D Fourier transform of each HerS map and attenuate spatial frequencies lower than $k = 0.1\,{\rm arcmin^{-1}}$ by a factor $(k/0.1)^3$, i.e.,

$$d_{\rm f}(x, y) = \begin{cases} \mathcal{F}^{-1} k \geq 0.1, & \hat{f}(l, m) \\ \mathcal{F}^{-1} k < 0.1, & \hat{f}(l, m)(k/0.1)^3 \end{cases}, \qquad (6)$$

where $d_{\rm f}$ is the filtered map, $\hat{f}(l, m)$ is the Fourier transform of the observed map with frequencies l and m in the x and y directions, respectively, and $k = \sqrt{l^2 + m^2}$.

The minimum filtering scale of $0.1\,{\rm arcmin^{-1}}$ was chosen because it is approximately the scale at which cirrus is seen to dominate the power spectrum in the SPIRE bands (e.g., Viero et al. 2013b). In Figure 6 we illustrate the effectiveness of this filtering on a 30 arcmin square region of the HerS 250 μm image that is badly affected by cirrus contamination.

Point sources are identified in the filtered 250 μm image using the IDL software package STARFINDER (Diolaiti et al. 2000). Sources are assumed to be exclusively point-like in the SPIRE images, with a point-spread function (PSF) described by a circular 2D Gaussian with FWHM of 18.15, 25.15 and 36.3 arcsec for 250, 350 and 500 μm, respectively. The effect of our Fourier filtering on the PSF is found to be very small, ≪ 1 per cent of the peak response, and so the assumption of Gaussian beams for our filtered maps remains valid. Any residual large-scale backgrounds in the SPIRE images are treated in STARFINDER by median smoothing the image with a 15 arcmin (150 pixel) window. While STARFINDER can operate in an "iterative" mode, detecting and removing sources at decreasing signal-to-noise ratio (SNR) thresholds, so as to allow the identification of faint sources in crowded regions, here we use a single pass of STARFINDER requiring peak SNR> 3 and $\rho_{\rm PSF}$, the correlation coefficient between the PSF and the candidate source, to be greater than 0.5. Running STARFINDER in this way across the full HerS 250 μm images results in the identification of 27,885 sources.

Finally, to perform source photometry we use a modified version of the De-blended SPIRE Photometry (DESPHOT) algorithm (Roseboom et al. 2010, 2012, henceforth R12; Wang et al., in prep.) developed for use on SPIRE data from the HerMES project (Oliver et al. 2012). The main advantage of this approach is that it deals with the source blending issue in a way more appropriate to SPIRE maps than STARFINDER, and produces consistent, band-merged SPIRE catalogues by using the input sources at the highest resolution band (250 μm) as

[28] The GASS second data release data server: http://www.astro.uni-bonn.de/hisurvey/gass/

a prior for the other SPIRE wavelengths.

While a complete description of how DESPHOT works is given in the above-listed papers, we briefly summarize the main points here. For source photometry, DESPHOT assumes that the map (or each map segment) can be described as the summation of the flux density from the n known sources in the map, i.e.,

$$\mathbf{d} = \sum_{i=1}^{n} \mathbf{P} f_i + \delta, \tag{7}$$

where $\mathbf{d}$ is the image data, $\mathbf{P}$ the PSF for source i, f_i the flux density of source i, and δ an unknown noise term. As discussed in Roseboom et al. (2010) a linear equation of this form will (as in § 3.2) have a maximum likelihood solution

$$\hat{\mathbf{f}} = (\mathbf{A}^{\mathrm{T}} \mathbf{N_d}^{-1} \mathbf{A})^{-1} \, \mathbf{A}^{\mathrm{T}} \mathbf{N_d}^{-1} \mathbf{d}, \tag{8}$$

where $\mathbf{A}$ is an m pixel by n source matrix that describes the PSF for each source in the map and $\mathbf{N_d}$ is the noise covariance matrix. The best non-negative solution for $\hat{\mathbf{f}}$ is found using the LASSO algorithm, as described in R12. As it is not computationally feasible to solve for the full set of $\sim$ 27,000 sources simultaneously the input list must be broken up into "groups" of sources that have significant overlap. In R12 this is accomplished by identifying high SNR "islands" in the SPIRE maps, but the HerS images are simply too big for this to be a reasonable option. Thus we group the DESPHOT input list with a friends-of-friends algorithm, specifically the SPHEREGROUP routine available as part of the SDSS IDLUTILS, using a linking length of 3 arcmin.

Taking the output from DESPHOT and cutting the catalogue to only those sources with an integrated SNR (i.e., $S/\Delta S$) of greater than five and reasonable residuals (i.e., $\chi^2 < 10$) results in a catalogue with 27,257 reliable 250 µm sources. Of these, 17,592 and 4,772 (at 350 and 500 µm, respectively) have 5σ flux density estimates at the other SPIRE wavelengths.

4.2. *Completeness and Reliability*

The completeness and reliability of the HerS catalogue is assessed using Monte Carlo techniques. The completeness is estimated by injecting grids of sources into the HerS maps and measuring the fraction that are detected (as 5σ sources) using the photometry pipeline. The input grids are matched to the output catalogue using a 6 arcsec matching radius, which we estimate will produce spurious matches between unassociated input mock sources and real SPIRE sources at a rate of 0.5%. As the HerS catalogue makes use of a 250 µm prior (i.e. we do not consider sources undetected at 250 µm) only the completeness at this wavelength is assessed. Table 1 presents the completeness as a function of 250 µm flux density for the HerS catalogue. It is worth noting that this completeness only considers the recoverability of sources at a given *true* flux density; at low SNR, the measured flux densities will be strongly affected by Eddington-type bias, i.e. $\langle S_{\rm obs}\rangle > \langle S_{\rm true}\rangle$. While the true impact of such flux boosting can only be assessed by taking into account the true distribution of flux densities (i.e., the number counts; Coppin et al. 2006), from our analysis we determine that $S_{250} \sim 40$ mJy is the faintest tested flux density at which the mean recovered flux density is equal to the injected value, i.e., $\langle S_{\rm obs}\rangle = \langle S_{\rm true}\rangle$.

Table 1
HerS completeness at 250 µm

S_{250} (mJy)	Completeness
20	0.06 ± 0.01
25	0.17 ± 0.03
30	0.30 ± 0.04
35	0.51 ± 0.05
40	0.70 ± 0.06
45	0.86 ± 0.06
50	0.95 ± 0.07

The reliability is estimated by taking jackknife realizations of the noise from deeper SPIRE imaging in the CDFS-SWIRE field. The HerMES observations of the CDFS-SWIRE field consist of eight scans of an 8 deg^2 region with SPIRE in fast scan mode. Thus we can produce four jackknife noise realizations at the depth of the HerS observations (2 scans) by producing maps from different pairs of scans in CDFS and subtracting away the eight scan maps. In order to assess the reliability of the HerS catalogue we run the pipeline on these noise-only maps. Across the four noise realizations (32 deg^2) we detect 32 spurious sources, giving a false positive rate of $1.0 \pm 0.2\,\mathrm{deg}^{-2}$. Thus across the 80 deg^2 of HerS we would expect 80 ± 16 spurious sources, or, considering our final catalog of 27,257 sources, 0.29 ± 0.06%.

5. CONCLUSION

We present and make publicly available the first sets of maps and catalogs from the *Herschel* Stripe 82 Survey. Maps at 250, 350, and 500 µm are made with the optimal mapmaker SANEPIC, which we demonstrate recovers emission on all scales that are in principle accessible. The survey encompasses approximately half of the 150 deg^2 of the deep SDSS stripe in which Galactic foregrounds are subdominant at submillimeter wavelengths (with HeLMS, described in Oliver et al. 2012, covering the other half). Approximately $\sim$ 10% of the HerS maps have significant foreground, with column densities $N_{\rm H} \gtrsim 4\times10^{21}\,\mathrm{cm}^{-2}$ and have been shown to be composed predominantly of local velocity clouds.

Merged three-color catalogs are constructed, after filtering, using DESPHOT (Roseboom et al. 2010) with 250 µm sources (extracted with STARFINDER) as the positional priors. We include sources with integrated SNR greater than 5, whose completeness is estimated to be 70% (Table 1), and false detection rate to be less than 1%.

HerS was designed with the intention of cross-correlating the maps with ancillary data — whether maps or catalogs of galaxies or clusters — to address a wide variety of questions. It was initially proposed to correlate with HETDEX Lyman α emitters (LAEs) at $1.8 < z < 3.5$ (e.g., Hill et al. 2008; Adams et al. 2011) with the aim of measuring the contribution to the CIB from that redshift range and infer the star-formation rate density through this critical epoch. Furthermore, combining that measurement with stellar masses of LAEs estimated from the SHELA/SpIES catalogs, specific star-formation rates, and the relationship of star-formation to halo mass at higher-z can be explored.

Other exciting projects that we intend to pursue in-

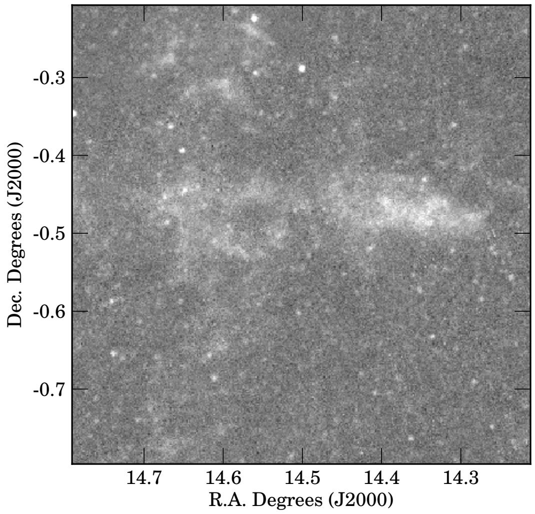

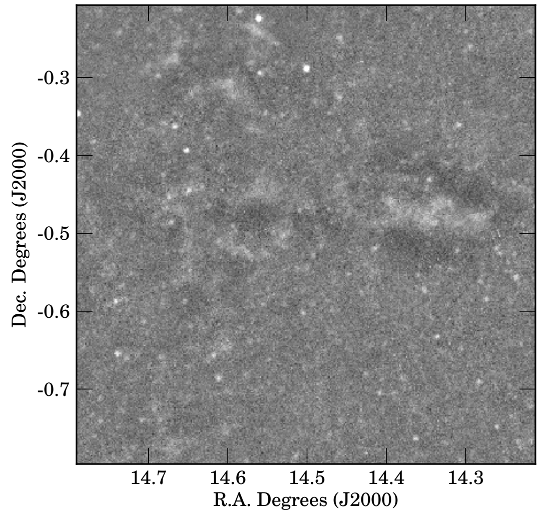

Figure 6. $36' \times 36'$ cutout from the HerS 250 μm map, in a region badly affected by Galactic cirrus. The cutout on the left is with no filtering, while the one on the right is with the tapered Fourier filtering described in the text. The effectiveness of the filter in removing large-scale features can be seen, but it also makes negative "bowls" around the brightest features.

clude: determining the correlation between HerS sources and clusters or cluster members, e.g., exploring the correlation of infrared emitting sources and clusters detected by ACT using the Sunyaev Zel'dovich (SZ) effect (Hasselfield et al. 2013); the lensing of the CMB by foreground structure traced by the CIB (Holder et al. 2013; Planck Collaboration et al. 2013; Hanson et al. 2013), and investigating the effect that the environment has on star-formation in sources identified as cluster members (Geach et al. 2012; Rykoff et al. 2013). SDSS/BOSS offers a wealth of galaxy and quasar (e.g., Ross et al. 2009; Pâris et al. 2012) populations for cross-correlation.

In addition to cross-correlations, single-object lensed or highly luminous high-redshift sources can be selected from the maps themselves. By linearly combining the maps, high-redshift "red peakers" (e.g., with $S_{250} < S_{350} < S_{500}$ at $z \gtrsim 3$; Riechers et al. 2013, Dowell et al. submitted) are identifiable. High-redshift groups and clusters can be selected as red overdensities (e.g., the *Planck* clumps; Clements et al., submitted), which alternatively can be used to clean the CIB from CMB maps to probe the damping tail of the CMB power spectrum (e.g., Hajian et al. 2012; Keisler et al. 2011; Reichardt et al. 2012; Sievers et al. 2013).

Studies focused on our Galaxy are possible as well. The large-scale fidelity of our maps, as demonstrated by the transfer function shown in Figure5, allows large-scale properties of cirrus and dense molecular regions to be fully reconstructed, while our relatively small beam means that finer structures can be separated out. And by correlating dust emission in the infrared with measurements from optical fibers pointed at "blank sky", we can recover the optical spectrum of the diffuse Galactic light to constrain the size distribution of Galactic dust (e.g. Brandt & Draine 2012).

Finally, future cosmological surveys such as the Dark Energy Survey (DES), Hyper Suprime-Cam (HSC), and the Large Synoptic Survey Telescope (LSST) will further enrich the density and variety of sources with which these submillimeter data can be cross-correlated, making this survey an integral component of an important Legacy field.

SPIRE has been developed by a consortium of institutes led by Cardiff Univ. (UK) and including: Univ. Lethbridge (Canada); NAOC (China); CEA, LAM (France); IFSI, Univ. Padua (Italy); IAC (Spain); Stockholm Observatory (Sweden); Imperial College London, RAL, UCL-MSSL, UKATC, Univ. Sussex (UK); and Caltech, JPL, NHSC, Univ. Colorado (USA). This development has been supported by national funding agencies: CSA (Canada); NAOC (China); CEA, CNES, CNRS (France); ASI (Italy); MCINN (Spain); SNSB (Sweden); STFC, UKSA (UK); and NASA (USA).

REFERENCES

Acquaviva, V., Hajian, A., Spergel, D. N., & Das, S. 2008, Phys. Rev. D, 78, 043514

Adams, J. J., Blanc, G. A., Hill, G. J., Gebhardt, K., Drory, N., Hao, L., Bender, R., Byun, J., et al. 2011, ApJS, 192, 5

Amblard, A., Cooray, A., Serra, P., Altieri, B., Arumugam, V., Aussel, H., Blain, A., Bock, J., et al. 2011, Nature, 470, 510

Berta, S., Magnelli, B., Nordon, R., Lutz, D., Wuyts, S., Altieri, B., Andreani, P., Aussel, H., et al. 2011, A&A, 532, A49

Béthermin, M., Dole, H., Lagache, G., Le Borgne, D., & Penin, A. 2011, A&A, 529, A4

Béthermin, M., Le Floc'h, E., Ilbert, O., Conley, A., Lagache, G., Amblard, A., Arumugam, V., Aussel, H., et al. 2012, A&A, 542, A58

Boulanger, F., Abergel, A., Bernard, J.-P., Burton, W. B., Desert, F.-X., Hartmann, D., Lagache, G., & Puget, J.-L. 1996, A&A, 312, 256

Bracco, A., Cooray, A., Veneziani, M., Amblard, A., Serra, P., Wardlow, J., Thompson, M. A., White, G., et al. 2011, MNRAS, 412, 1151

Brandt, T. D. & Draine, B. T. 2012, ApJ, 744, 129

Chapin, E. L., Chapman, S. C., Coppin, K. E., Devlin, M. J., Dunlop, J. S., Greve, T. R., Halpern, M., Hasselfield, M. F., et al. 2011, MNRAS, 411, 505

Devlin, M. J., Ade, P. A. R., Aretxaga, I., Bock, J. J., Chapin, E. L., Griffin, M., Gundersen, J. O., Halpern, M., et al. 2009, Nature, 458, 737

Diolaiti, E., Bendinelli, O., Bonaccini, D., Close, L., Currie, D., & Parmeggiani, G. 2000, A&AS, 147, 335
Dole, H., Lagache, G., Puget, J.-L., Caputi, K. I., Fernández-Conde, N., Le Floc'h, E., Papovich, C., Pérez-González, P. G., et al. 2006, A&A, 451, 417
Eales, S., Dunne, L., Clements, D., Cooray, A., de Zotti, G., Dye, S., Ivison, R., Jarvis, M., et al. 2010, PASP, 122, 499
Eisenstein, D. J., Weinberg, D. H., Agol, E., Aihara, H., Allende Prieto, C., Anderson, S. F., Arns, J. A., Aubourg, É., et al. 2011, AJ, 142, 72
Emerson, J. P., Sutherland, W. J., McPherson, A. M., Craig, S. C., Dalton, G. B., & Ward, A. K. 2004, The Messenger, 117, 27
Fixsen, D. J., Dwek, E., Mather, J. C., Bennett, C. L., & Shafer, R. A. 1998, ApJ, 508, 123
Geach, J. E., Chapin, E. L., Coppin, K. E. K., Dunlop, J. S., Halpern, M., Smail, I., van der Werf, P., Serjeant, S., et al. 2012, ArXiv e-prints
Geach, J. E., Chapin, E. L., Coppin, K. E. K., Dunlop, J. S., Halpern, M., Smail, I., Werf, P. v. d., Serjeant, S., et al. 2013, MNRAS, 432, 53
Glenn, J., Conley, A., Béthermin, M., Altieri, B., Amblard, A., Arumugam, V., Aussel, H., Babbedge, T., et al. 2010, MNRAS, 409, 109
Griffin, M. J., Abergel, A., Abreu, A., Ade, P. A. R., André, P., Augueres, J.-L., Babbedge, T., Bae, Y., et al. 2010, A&A, 518, L3
Hajian, A., Viero, M. P., Addison, G., Aguirre, P., Appel, J. W., Battaglia, N., Bock, J. J., Bond, J. R., et al. 2012, ApJ, 744, 40
Hanson, D., Hoover, S., Crites, A., Ade, P. A. R., Aird, K. A., Austermann, J. E., Beall, J. A., Bender, A. N., et al. 2013, ArXiv e-prints
Hasselfield, M., Hilton, M., Marriage, T. A., Addison, G. E., Barrientos, L. F., Battaglia, N., Battistelli, E. S., Bond, J. R., et al. 2013, ArXiv e-prints
Hauser, M. G. & Dwek, E. 2001, ARA&A, 39, 249
Hill, G. J., Gebhardt, K., Komatsu, E., Drory, N., MacQueen, P. J., Adams, J., Blanc, G. A., Koehler, R., et al. 2008, in Astronomical Society of the Pacific Conference Series, Vol. 399, Panoramic Views of Galaxy Formation and Evolution, ed. T. Kodama, T. Yamada, & K. Aoki, 115
Hodge, J. A., Becker, R. H., White, R. L., Richards, G. T., & Zeimann, G. R. 2011, AJ, 142, 3
Holder, G. P., Viero, M. P., Zahn, O., Aird, K. A., Benson, B. A., Bhattacharya, S., Bleem, L. E., Bock, J., et al. 2013, ArXiv e-prints
Kalberla, P. M. W., McClure-Griffiths, N. M., Pisano, D. J., Calabretta, M. R., Ford, H. A., Lockman, F. J., Staveley-Smith, L., Kerp, J., et al. 2010, A&A, 521, A17+
Keisler, R., Reichardt, C. L., Aird, K. A., Benson, B. A., Bleem, L. E., Carlstrom, J. E., Chang, C. L., Cho, H. M., et al. 2011, ApJ, 743, 28
Kurczynski, P., Gawiser, E., Huynh, M., Ivison, R. J., Treister, E., Smail, I., Blanc, G. A., Cardamone, C. N., et al. 2012, ApJ, 750, 117
Levenson, L., Marsden, G., Zemcov, M., Amblard, A., Blain, A., Bock, J., Chapin, E., Conley, A., et al. 2010, MNRAS, 409, 83
Lutz, D., Poglitsch, A., Altieri, B., Andreani, P., Aussel, H., Berta, S., Bongiovanni, A., Brisbin, D., et al. 2011, A&A, 532, A90
Marsden, G., Ade, P. A. R., Bock, J. J., Chapin, E. L., Devlin, M. J., Dicker, S. R., Griffin, M., Gundersen, J. O., et al. 2009, ApJ, 707, 1729
McClure-Griffiths, N. M., Pisano, D. J., Calabretta, M. R., Ford, H. A., Lockman, F. J., Staveley-Smith, L., Kalberla, P. M. W., Bailin, J., et al. 2009, ApJS, 181, 398
Miyazaki, S., Komiyama, Y., Nakaya, H., Kamata, Y., Doi, Y., Hamana, T., Karoji, H., Furusawa, H., et al. 2012, in Society of Photo-Optical Instrumentation Engineers (SPIE) Conference Series, Vol. 8446, Society of Photo-Optical Instrumentation Engineers (SPIE) Conference Series
Negrello, M., Hopwood, R., De Zotti, G., Cooray, A., Verma, A., Bock, J., Frayer, D. T., Gurwell, M. A., et al. 2010, Science, 330, 800
Netterfield, C. B., Ade, P. A. R., Bock, J. J., Chapin, E. L., Devlin, M. J., Griffin, M., Gundersen, J. O., Halpern, M., et al. 2009, ApJ, 707, 1824
Nguyen, H. T., Schulz, B., Levenson, L., Amblard, A., Arumugam, V., Aussel, H., Babbedge, T., Blain, A., et al. 2010, A&A, 518, L5+
Oliver, S. J., Bock, J., Altieri, B., Amblard, A., Arumugam, V., Aussel, H., Babbedge, T., Beelen, A., et al. 2012, MNRAS, 424, 1614
Oliver, S. J., Wang, L., Smith, A. J., Altieri, B., Amblard, A., Arumugam, V., Auld, R., Aussel, H., et al. 2010, A&A, 518, L21+
Ott, S. 2010, in Astronomical Society of the Pacific Conference Series, Vol. 434, Astronomical Data Analysis Software and Systems XIX, 139–+
Papovich, C. J., Gebhardt, K., Behroozi, P., Bender, R., Blanc, G. A., Ciardullo, R., DePoy, D., de Jong, R., et al. 2012, in American Astronomical Society Meeting Abstracts, Vol. 219, American Astronomical Society Meeting Abstracts #219, 424.09
Pâris, I., Petitjean, P., Aubourg, É., Bailey, S., Ross, N. P., Myers, A. D., Strauss, M. A., Anderson, S. F., et al. 2012, A&A, 548, A66
Pascale, E., Ade, P. A. R., Bock, J. J., Chapin, E. L., Devlin, M. J., Dye, S., Eales, S. A., Griffin, M., et al. 2009, ApJ, 707, 1740
Patanchon, G., Ade, P. A. R., Bock, J. J., Chapin, E. L., Devlin, M. J., Dicker, S., Griffin, M., Gundersen, J. O., et al. 2008, ApJ, 681, 708
Pilbratt, G. L., Riedinger, J. R., Passvogel, T., Crone, G., Doyle, D., Gageur, U., Heras, A. M., Jewell, C., et al. 2010, A&A, 518, L1
Planck Collaboration, Abergel, A., Ade, P. A. R., Aghanim, N., Arnaud, M., Ashdown, M., Aumont, J., Baccigalupi, C., et al. 2011a, A&A, 536, A24
Planck Collaboration, Ade, P. A. R., Aghanim, N., Armitage-Caplan, C., Arnaud, M., Ashdown, M., Atrio-Barandela, F., Aumont, J., et al. 2013, ArXiv e-prints
Planck Collaboration, Ade, P. A. R., Aghanim, N., Arnaud, M., Ashdown, M., Aumont, J., Baccigalupi, C., Balbi, A., et al. 2011b, A&A, 536, A19
—. 2011c, A&A, 536, A18
Puget, J.-L., Abergel, A., Bernard, J.-P., Boulanger, F., Burton, W. B., Desert, F.-X., & Hartmann, D. 1996, A&A, 308, L5+
Reichardt, C. L., Shaw, L., Zahn, O., Aird, K. A., Benson, B. A., Bleem, L. E., Carlstrom, J. E., Chang, C. L., et al. 2012, ApJ, 755, 70
Richards, G., Lacy, M., Strauss, M., Spergel, D., Anderson, S., Bauer, F., Bochanski, J., Brandt, N., et al. 2012, Spitzer Proposal, 90045
Riechers, D. A., Bradford, C. M., Clements, D. L., Dowell, C. D., Pérez-Fournon, I., Ivison, R. J., Bridge, C., Conley, A., et al. 2013, Nature, 496, 329
Roseboom, I. G., Ivison, R. J., Greve, T. R., Amblard, A., Arumugam, V., Auld, R., Aussel, H., Bethermin, M., et al. 2012, MNRAS, 419, 2758
Roseboom, I. G., Oliver, S. J., Kunz, M., Altieri, B., Amblard, A., Arumugam, V., Auld, R., Aussel, H., et al. 2010, MNRAS, 409, 48
Ross, N. P., Shen, Y., Strauss, M. A., Vanden Berk, D. E., Connolly, A. J., Richards, G. T., Schneider, D. P., Weinberg, D. H., et al. 2009, ApJ, 697, 1634
Rykoff, E. S., Rozo, E., Busha, M. T., Cunha, C. E., Finoguenov, A., Evrard, A., Hao, J., Koester, B. P., et al. 2013, ArXiv e-prints
Sievers, J. L., Hlozek, R. A., Nolta, M. R., Acquaviva, V., Addison, G. E., Ade, P. A. R., Aguirre, P., Amiri, M., et al. 2013, ArXiv e-prints
Vieira, J. D., Marrone, D. P., Chapman, S. C., De Breuck, C., Hezaveh, Y. D., Weiβ, A., Aguirre, J. E., Aird, K. A., et al. 2013, Nature, 495, 344
Viero, M. P., Ade, P. A. R., Bock, J. J., Chapin, E. L., Devlin, M. J., Griffin, M., Gundersen, J. O., Halpern, M., et al. 2009, ApJ, 707, 1766
Viero, M. P., Moncelsi, L., Mentuch, E., Buitrago, F., Bauer, A. E., Chapin, E. L., Conselice, C. J., Devlin, M. J., et al. 2012, MNRAS, 2405

Viero, M. P., Moncelsi, L., Quadri, R. F., Arumugam, V., Assef, R. J., Bethermin, M., Bock, J., Bridge, C., et al. 2013a, ArXiv e-prints
Viero, M. P., Wang, L., Zemcov, M., Addison, G., Amblard, A., Arumugam, V., Aussel, H., Béthermin, M., et al. 2013b, ApJ, 772, 77
Wang, L., Farrah, D., Oliver, S. J., Amblard, A., Béthermin, M., Bock, J., Conley, A., Cooray, A., et al. 2013, MNRAS, 431, 648
Wardlow, J. L., Cooray, A., De Bernardis, F., Amblard, A., Arumugam, V., Aussel, H., Baker, A. J., Béthermin, M., et al. 2012, ArXiv e-prints
Weiß, A., Kovács, A., Coppin, K., Greve, T. R., Walter, F., Smail, I., Dunlop, J. S., Knudsen, K. K., et al. 2009, ApJ, 707, 1201